Modelling of surface waves on a THz antenna detected by a near-field probe

Michele Natrella, Oleg Mitrofanov, Raimund Mueckstein, Chris Graham, Cyril C. Renaud, and Alwyn J. Seeds*

Department of Electronic & Electrical Engineering, University College London, Torrington Place, London, WC1E 7JE, UK

**a.seeds@ee.ucl.ac.uk*

Abstract: We have modelled the experimental system based on the sub-wavelength aperture probe employed in our previous work for terahertz (THz) surface plasmon wave imaging on a bowtie antenna. For the first time we demonstrate the accuracy of the proposed interpretation of the images mapped by the probe. The very good agreement between numerical and experimental results proves that the physical quantity detected by the probe is the spatial derivative of the electric field normal component. The achieved understanding of the near-field probe response allows now a correct interpretation of the images and the distribution of the electric field to be extracted. We have also carried out the first assessment of the probe invasiveness and found that the pattern of the surface plasmon wave on the antenna is not modified significantly by the proximity of the probe. This makes the experimental system an effective tool for near-field imaging of THz antennas and other metallic structures.

OCIS codes: (240.6680) Surface plasmons; (110.6795) Terahertz imaging; (180.4243) Near-field microscopy; (320.7100) Ultrafast measurements.

References and links

1. A. J. L. Adam, "Review of near-field terahertz measurement methods and their applications," J. Infrared Milli. Terahz. Waves **32**(8-9), 976–1019 (2011).
2. K. Yang, G. David, J. Yook, I. Papapolymerou, L. P. B. Katehi, and J. F. Whitaker, "Electrooptic mapping and finite-element modeling of the near-field pattern of a microstrip patch antenna," IEEE Trans. Microw. Theory Tech. **48**(2), 288–294 (2000).
3. M. A. Seo, A. J. L. Adam, J. H. Kang, J. W. Lee, S. C. Jeoung, Q. H. Park, P. C. M. Planken, and D. S. Kim, "Fourier-transform terahertz near-field imaging of one-dimensional slit arrays: mapping of electric-field-, magnetic-field-, and Poynting vectors," Opt. Express **15**(19), 11781–11789 (2007).
4. A. J. Huber, F. Keilmann, J. Wittborn, J. Aizpurua, and R. Hillenbrand, "Terahertz near-field nanoscopy of mobile carriers in single semiconductor nanodevices," Nano Lett. **8**(11), 3766–3770 (2008).
5. R. Mueckstein and O. Mitrofanov, "Imaging of terahertz surface plasmon waves excited on a gold surface by a focused beam," Opt. Express **19**(4), 3212–3217 (2011).
6. K. Ishihara, K. Ohashi, T. Ikari, H. Minamide, H. Yokoyama, J. Shikata, and H. Ito, "Terahertz-wave near-field imaging with subwavelength resolution using surface-wave-assisted bow-tie aperture," Appl. Phys. Lett. **89**(20), 201120 (2006).
7. M. Walther and A. Bitzer, "Electromagnetic wave propagation close to microstructures studied by time and phase-resolved THz near-field imaging," J. Infrared Milli. Terahz. Waves **32**(8-9), 1020–1030 (2011).
8. R. Mueckstein, C. Graham, C. C. Renaud, A. J. Seeds, J. A. Harrington, and O. Mitrofanov, "Imaging and analysis of THz surface plasmon polariton waves with the integrated sub-wavelength aperture probe," J. Infrared Milli. Terahz. Waves **32**(8-9), 1031–1042 (2011).
9. Q. H. Park, "Optical antennas and plasmonics," Contemp. Phys. **50**(2), 407–423 (2009).
10. E. Cubukcu, N. Yu, E. J. Smythe, L. Diehl, K. B. Crozier, and F. Capasso, "Plasmonic laser antennas and related devices," IEEE J. Sel. Top. Quantum Electron. **14**(6), 1448–1461 (2008).
11. P. Ghenuche, S. Cherukulappurath, T. H. Taminiau, N. F. van Hulst, and R. Quidant, "Spectroscopic mode mapping of resonant plasmon nanoantennas," Phys. Rev. Lett. **101**(11), 116805 (2008).
12. E. S. Barnard, R. A. Pala, and M. L. Brongersma, "Photocurrent mapping of near-field optical antenna resonances," Nat. Nanotechnol. **6**(9), 588–593 (2011).
13. A. Kinkhabwala, Z. Yu, S. Fan, Y. Avlasevich, K. Müllen, and W. E. Moerner, "Large single-molecule fluorescence enhancements produced by a bowtie nanoantenna," Nat. Photonics **3**(11), 654–657 (2009).

#167707 - $15.00 USD Received 1 May 2012; revised 13 Jun 2012; accepted 14 Jun 2012; published 29 Jun 2012

14. O. Mitrofanov, M. Lee, J. W. P. Hsu, I. Brener, R. Harel, J. F. Federici, J. D. Wynn, L. N. Pfeiffer, and K. W. West, "Collection-mode near-field imaging with 0.5-THz pulses," IEEE J. Sel. Top. Quantum Electron. **7**(4), 600–607 (2001).
15. O. Mitrofanov, R. Harel, M. Lee, L. N. Pfeiffer, K. West, J. D. Wynn, and J. Federici, "Study of single-cycle pulse propagation inside a terahertz near-field probe," Appl. Phys. Lett. **78**(2), 252 (2001).
16. M. A. Ordal, L. L. Long, R. J. Bell, S. E. Bell, R. R. Bell, R. W. Alexander, Jr., and C. A. Ward, "Optical properties of the metals Al, Co, Cu, Au, Fe, Pb, Ni, Pd, Pt, Ag, Ti, and W in the infrared and far infrared," Appl. Opt. **22**(7), 1099–1119 (1983).
17. F. Garet and L. Duvillaret, "THz time-domain spectroscopy of nanometric-thick gold layers," Digest of the 2004 Joint 29th 467-468 (2004).
18. D. Grischkowsky, S. Keiding, M. van Exter, and C. Fattinger, "Far-infrared time-domain spectroscopy with terahertz beams of dielectrics and semiconductors," J. Opt. Soc. Am. B **7**(10), 2006–2015 (1990).
19. M. Nagai, K. Tanaka, H. Ohtake, T. Bessho, T. Sugiura, T. Hirosumi, and M. Yoshida, "Generation and detection of terahertz radiation by electro-optical process in GaAs using 1.56 μm fiber laser pulses," Appl. Phys. Lett. **85**(18), 3974 (2004).
20. O. Mitrofanov, L. N. Pfeiffer, and K. West, "Generation of low-frequency components due to phase-amplitude modulation of subcycle far-infrared pulses in near-field diffraction," Appl. Phys. Lett. **81**(9), 1579 (2002).

1. Introduction

Application of the near-field scanning probe microscopy method at terahertz (THz) frequencies (λ = 30-1000 μm) has enabled studies of a range of scientific questions [1]. The method allows spatial resolution to be improved beyond the diffraction limit, as well as detecting evanescent components of the THz field [1–8]. This capability is particularly suitable for studies of electromagnetic fields in the near-field region of antennas. Several investigations of THz and optical antennas have been performed recently [8–13]. Antennas provide a possibility to concentrate the electric field in a sub-wavelength region and application of optical antennas enabled challenging studies, such as spectroscopic investigation of individual molecules. The concentrated field in the antenna gap however depends sensitively on the antenna geometry and experimental images of the field distribution in the near-field zone of the antenna are essential for evaluating the antenna performance.

Understanding of the near-field probe interaction with objects is central to the correct interpretation of images. In general, near-field images represent a convolution of the optical field with the near-field probe spatial response, which is often a complex function of the electric field vector and its derivatives, especially if probe modulation techniques are used to improve the method sensitivity. Near-field probes also disturb the optical field and it is important to understand the probe invasiveness.

One of the probes developed for THz near-field microscopy, the integrated sub-wavelength aperture probe [14], was recently shown to be sensitive to THz surface plasmon waves [5,8]. The probe provides the possibility of mapping THz surface plasmon waves with spatial resolution better than 10 microns [14], and to track the wave propagation in time [5,8]. To enable precise analysis of the surface wave phenomena, an understanding of the probe response is essential.

Experimental results discussed in [8] suggested that the near-field images represent the in-plane spatial derivative of the surface plasmon field distribution. The spatial derivative nature implies that near-field images may show patterns that are different from the surface plasmon field distribution. For example, a uniform travelling wave is displayed with a phase shift and a standing surface wave confined on small metallic objects, such as an antenna, may show a change in the detected pattern symmetry. The detected field amplitude may also depend on the direction of the surface wave propagation. Analysis of near-field images of test objects suggested that these effects are present and a simplified coupling mechanism was introduced to explain the near-field probe response [8].

To verify the model of the near-field probe response, here we evaluate the response numerically; the computational approach also allows a preliminary assessment of the question of probe invasiveness. The near-field response is analysed by considering surface plasmon waves on the surface of a bow-tie antenna and comparing the results with experimental images collected by the near-field probe. Our numerical results confirm that the experimental images display the spatial derivative of the surface plasmon field formed on metallic surfaces

#167707 - $15.00 USD Received 1 May 2012; revised 13 Jun 2012; accepted 14 Jun 2012; published 29 Jun 2012

and show similar field patterns on the surface of the bow-tie antenna with and without the near-field probe present. The invasiveness of the probe only becomes evident near the edges of the antenna. The results show that the integrated sub-wavelength aperture probe can be applied to imaging of surface plasmon waves on patterned metallic surfaces, such as antennas and metamaterials.

2. Integrated sub-wavelength aperture near-field probe

In the experimental system, the integrated sub-wavelength aperture probe is positioned within several microns of the sample surface (Fig. 1(a)). The sample is illuminated from the substrate side by an unfocused THz beam formed by a cylindrical waveguide [8]. The probe contains a GaAs photoconductive antenna detector attached to a transparent substrate (the antenna and the low temperature grown GaAs layer facing the substrate), and a flat thin metallic screen (gold, 600nm) deposited on the back side of the thinned GaAs layer [14]. The screen has a 20μm × 20μm aperture in the centre of the antenna region (Fig. 1(a), inset). Details of the probe design, fabrication and its performance with a THz time-domain system are described in [14,15]. The probe detects only a local value of the THz field in the region of the aperture. A field distribution near the sample surface therefore can be mapped by scanning the sample with respect to the probe. In order to keep the illumination field constant during the scan, the waveguide is attached rigidly to the sample.

The effect of the probe on the sample is equivalent to the effect of an infinite metallic plane positioned parallel to the sample surface, because the screen is large in size (~2mm × 6mm) compared with the bowtie antenna and the illuminating beam. We can also assume that the aperture in the screen does not perturb the field distribution because the aperture is significantly smaller than the wavelength and the sample.

The metallic screen can support surface plasmon waves excited within the sample. Consider a sample that contains a planar bow-tie antenna on a dielectric substrate and plasmon waves excited on the antenna surface by a THz wave incident from the substrate side. The incident wave forms an electric field pattern, which represents travelling and standing surface plasmon waves on the antenna surface (Fig. 1(b)). The electric field vector is oriented perpendicular to the surface in the close proximity to the surface and it decays exponentially away from the surface. It is important to consider the effect of the metallic plane of the probe positioned parallel to the antenna surface. Although the field distribution near the antenna is in general affected by the metallic surface, the pattern of the surface plasmon wave is expected to remain similar to the original pattern because the original surface plasmon field satisfies the boundary conditions imposed by the metallic plane.

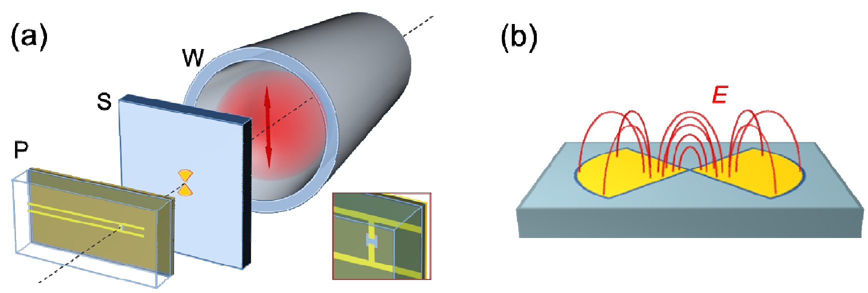

Fig. 1. (a) Schematic diagram of the experimental setup showing the integrated near-field probe (P), the bow-tie antenna sample (S), and the THz waveguide (W). The inset shows an enlarged antenna section of the probe. (b) Schematic diagram of the bow-tie antenna sample showing the electric field lines forming on the antenna surface when it is illuminated by the THz beam from the substrate side.

The choice of the bowtie antenna as a sample to analyse in our experiment is justified by its size and shape. The bowtie antenna employed in this work (radius of 300μm) offers a large enough area for correct detection of surface waves; the spectral content of the THz pulse that

#167707 - $15.00 USD Received 1 May 2012; revised 13 Jun 2012; accepted 14 Jun 2012; published 29 Jun 2012

we use to excite the antenna (1.4 to 2.1 THz) contains frequencies significantly higher than the half-lambda resonance of the bowtie antenna and can therefore produce identifiable patterns. The shape of the antenna enables formation of interference patterns due to reflections travelling from multiple directions. The antenna is also much bigger than the probe aperture, which defines the spatial resolution. We note that detection of surface waves on metallic structures with features comparable in size to the aperture can be ambiguous because, near the edges, the incident field is also detected by the probe.

The sub-wavelength aperture allows a small amount of the surface plasmon wave to couple through it as an evanescent field. This field is measured by the THz photoconductive antenna detector, however the relationship between the detected field and the surface plasmon wave field in the vicinity of the aperture is not direct. According to the coupling mechanism proposed in [8], the in-plane variation of the surface plasmon field causes a potential difference on the opposite edges of the aperture. The corresponding electric field is in the plane of the aperture and it is proportional to the in-plane gradient of the surface plasmon wave distribution. The THz photoconductive antenna is also oriented in the plane of the aperture and therefore the field coupled through the aperture can be detected by the antenna as a projection of the gradient vector on the antenna axis. The mapping of the field distribution therefore results in an image that combines the surface plasmon wave pattern on the antenna and the incident field distribution.

In the next section we discuss results of numerical simulations to model the integrated near-field probe by a metallic plane positioned at distance of 3 μm away from the bow-tie antenna sample. The surface plasmon field formed by a modelled THz pulse between the antenna surface and the probe surface will be compared to the surface plasmon field formed without the metallic plane present. The results of the simulations will allow verification of the coupling mechanism and a first evaluation of the invasiveness of the near-field probe.

3. Numerical modelling and simulation

In our previous work we proposed the hypothesis, supported only by a simplified explanation of the coupling mechanism and experimental clues, suggesting that the physical quantity detected by the probe is in fact the spatial derivative of the electric field z component with respect to the direction parallel to the dipole inside the probe (which in our experiment coincides with the y axis). With this simulation we intend to provide, for the first time, conclusive evidence of the accuracy of our hypothesis. For this purpose we model the experimental system based on the sub-wavelength aperture probe and replicate numerically the windowed time domain experiment described in [8]. All numerical simulations are performed using the commercial software CST Microwave Studio and all data pre- and post-processing is carried out in MATLAB.

An overview of the model structure is shown in Fig. 2(a), while Fig. 2(b) illustrates the plane wave employed as excitation source. The bow-tie antenna chip has been modelled following the system employed in the laboratory experiment [8], with the following geometrical parameters: 1) angle of 90°; 2) radius of 300 μm; 3) gap of 10 μm in the midpoint; 4) lossy gold thickness of 300 nm; 5) loss free GaAs substrate height, width and thickness of 1460 μm, 1290 μm and 150 μm respectively. The properties of gold [16,17] and GaAs [18,19] are loaded into the simulation model from a CST native library. The basic properties of the two materials are shown in Table 1 and the geometrical parameters are listed in Table 2 together with their values.

#167707 - $15.00 USD Received 1 May 2012; revised 13 Jun 2012; accepted 14 Jun 2012; published 29 Jun 2012

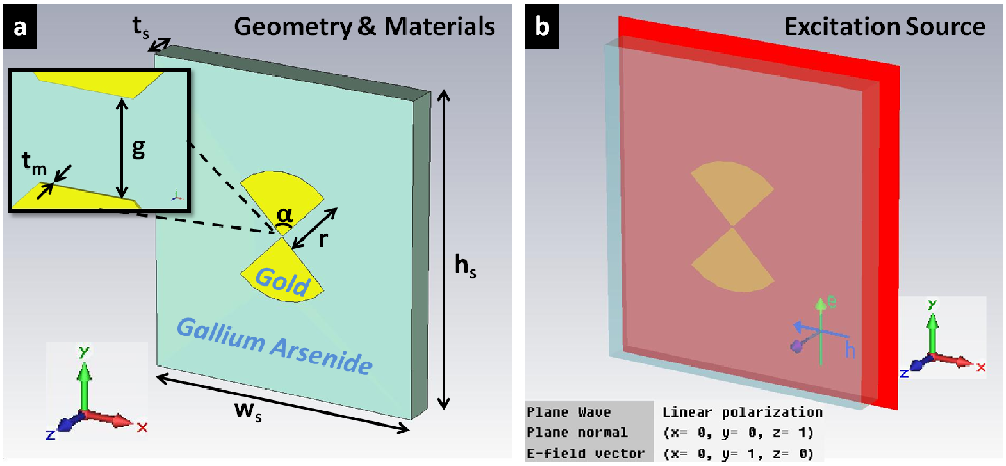

Fig. 2. (a) Model structure and materials. (b) Plane wave employed as excitation source.

The modelled probe response must not be affected by reflections inside the substrate or border effects originating at the edges of the substrate. Therefore the size of the substrate has to be large enough to allow the waveform coming from the excitation source to pass over the antenna undisturbed. Two other important factors to be taken into account when deciding the substrate size, concern the computational load and the accuracy of the simulation. If the substrate is too large the accuracy of the results is reduced unless an extremely high number of mesh cells is set for the model with a consequent soaring computational load. In order to honour all these requirements the size designed for the substrate is the smallest possible that still prevents reflections and border effects from affecting the probe within the time window in which its response is analysed.

The presence of the probe over the bow-tie antenna is taken into account by placing an infinite gold plane that acts as z_{max} boundary condition, 3 μm above the substrate. All the other boundary conditions are set to "open (add space)" meaning that some space between the faces of the substrate and the boundary box is filled with background material, air in this case.

In order to further reduce the computational load, two symmetry planes are considered: 1) the [x, z] plane is set to "electric wall" which forces the tangential component of the electric field to be equal to zero; 2) the [y, z] plane is set to "magnetic wall" which forces the tangential component of the magnetic field to be equal to zero.

Table 1. Physical Properties of the Materials Used in the Model

		Material Properties		
Material	**Type**	**Dielectric Permittivity**	**Magnetic Permeability**	**Electrical Conductivity**
Gold	Lossy Metal	–	1	4.561×10^7 [S/m] [16,17]
Gallium Arsenide	Loss Free Isotropic Dielectric	12.94 [18,19]	1	–

#167707 - $15.00 USD Received 1 May 2012; revised 13 Jun 2012; accepted 14 Jun 2012; published 29 Jun 2012

Table 2. List of the Geometrical Parameters

Geometrical Parameters		
Name	**Value**	**Unit Measure**
r	300	μm
α	90	deg
t_m	300	nm
g	10	μm
t_s	150	μm
h_s	1460	μm
w_s	1290	μm

As shown in Fig. 2(b) the excitation source is modelled as a plane wave propagating forward along the z axis and linearly polarised in the y axis. In order to match the modelling as closely as possible to reality, the waveform employed for the numerical simulation is calculated from the actual signal detected in the laboratory experiment [8], whose samples are shown in Fig. 3 with black circles, and is imported into the model as an ASCII file. A pre-processing of the detected samples is necessary to make the signal compatible with the software requirements, and consists of four steps: 1) up-sampling to adapt the coarse detected signal to the much finer time step used in the CST default waveforms; 2) removing the abrupt truncations at the start and end points of the function as they would introduce ripples in the frequency domain; this is done by fitting the signal extremities to appropriate sinusoidal signals rapidly decaying to zero; 3) scaling to give the function an amplitude compatible with the typical values employed in the CST default waveforms; 4) removing a small DC component present in the waveform detected in the lab experiment. The experimental samples of the original waveform were detected on the same face of the substrate where the bow-tie antenna lies, but far enough from the antenna and the borders of the substrate to avoid any interference from the antenna response, the reflections inside the substrate or the border effects; the same detection has also been performed numerically to make sure that the signal time of flight and the temporal derivative effect introduced by the probe on the incident field tangent component [8] are properly taken into account. The waveform depicted as a continuous blue line in Fig. 3 represents the signal detected in the simulation on the same plane containing the antenna but far away from any interference.

#167707 - $15.00 USD Received 1 May 2012; revised 13 Jun 2012; accepted 14 Jun 2012; published 29 Jun 2012

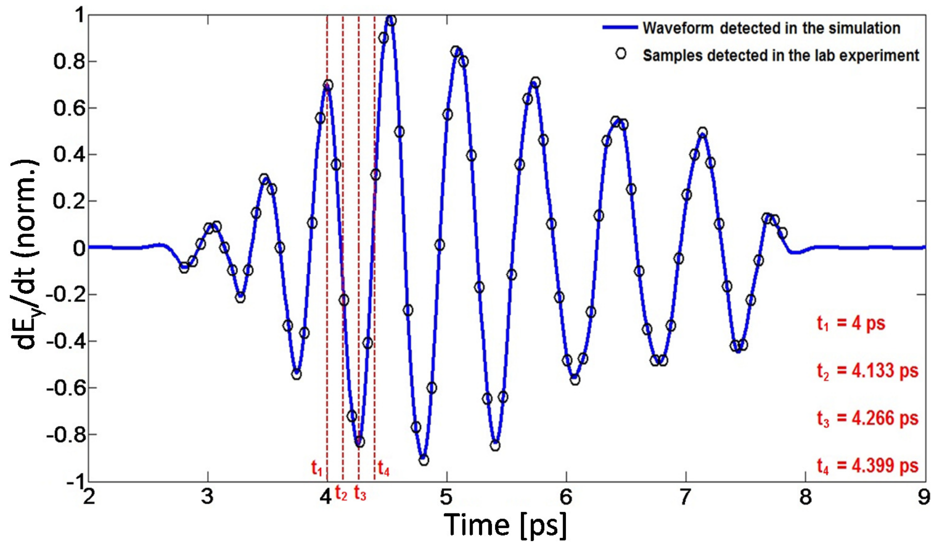

Fig. 3. The black circles are the samples of the actual signal detected in the laboratory. The waveform depicted as a continuous blue line represents the signal in the simulation arriving at the same detection point. As explained in [8], far away from any interference, the probe detects the time derivative of the transverse incident field (E_y in this work). The instants t_1, t_2, t_3, t_4 are the times at which the field was mapped in the laboratory experiment.

The instants t_1, t_2, t_3, t_4 highlighted in Fig. 3 are the times at which the field was mapped in the laboratory experiment. Thus, in order to compare the experimental and the numerical results, the simulation has to calculate the electric field on the surface of the antenna over a lapse of time containing the instants t_1, t_2, t_3, t_4. The values of the z component of the electric field calculated 3 µm over the substrate in the instants t_1, t_2, t_3, t_4 are then exported in ASCII files with x step and y step of 1 µm. These ASCII files are then imported in MATLAB to calculate the spatial derivative. The major goal of this work is in fact to demonstrate that the physical quantity detected by the probe is the spatial derivative of the electric field z component on the surface of the antenna. Finally, in order to carry out a comparison with the measurement results, the matrices containing the electric field derivative values are mapped and saved as images.

4. Results and discussion

The comparison between the measurement and the numerical calculation results is shown in Fig. 4. The images in the first row represent the patterns mapped with the data collected in the laboratory experiment; in these images we plot the current detected at the output of the photoconductive antenna inside the sub-wavelength aperture probe. The images in the second row are the results of the CST simulation followed by the MATLAB post-processing and display the spatial derivative of the electric field z component. Since the probe in general detects the combination of the normal and the tangent components, the comparison is valid only on the metallic surface of the bowtie antenna, where no incident field is present.

#167707 - $15.00 USD Received 1 May 2012; revised 13 Jun 2012; accepted 14 Jun 2012; published 29 Jun 2012

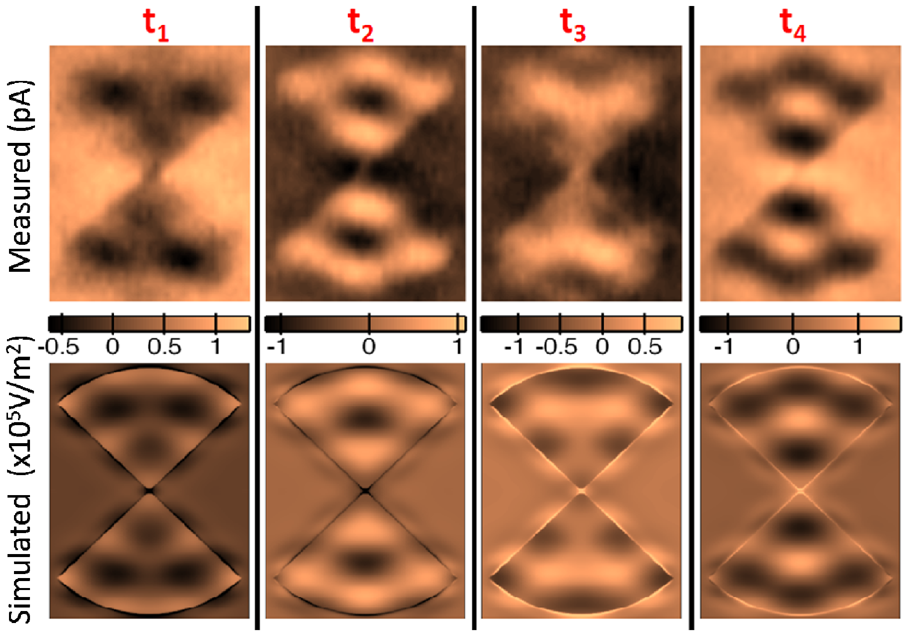

Fig. 4. Comparison between the patterns mapped in the laboratory experiment [8] and the patterns obtained through CST simulation and MATLAB post-processing. The experimental images depict the current detected at the output of the photoconductive antenna inside the probe. The numerical images depict the spatial derivative dE_z/dy of the electric field z component. Each image covers an area of 460 x 620 μm^2.

The good agreement between numerical calculation and experimental results demonstrates that the physical quantity detected by the probe is indeed the spatial derivative of the electric field of the surface wave. It is important to note that the experimental images obtained with the sub-wavelength aperture probe are not expected to depend on the aperture size as long as the aperture is significantly smaller than the wavelength and smaller than the sample features. It was shown previously that an incident THz pulse (E_x) detected by the sub-wavelength aperture probes with different aperture sizes, shows the same waveform shape [20], i.e. the probe frequency response scales by a constant if the aperture size is varied. Based on the coupling model proposed in [8], we expect that the frequency response to the E_z component, similarly to the response to E_x component, maintains its functional frequency dependence if the aperture size is varied. As a consequence, the detected images and time-domain waveforms are not expected to depend on the probe aperture size. This conclusion is consistent with the result of our modelling in which we make no assumption about the aperture size except that it is substantially smaller than the wavelength. Smaller apertures, of course, improve the spatial resolution, whereas the patterns themselves are not affected. We note that the amplitude of the detected signal decreases with the aperture size.

In Fig. 5 we also show the good agreement between the time-domain waveform detected in the laboratory experiment (black circles) on the metal of the antenna at a distance of 175 μm from the centre of the gap and the time-domain waveform of the electric field z component spatial derivative $dE_z(t)/dy$ obtained in the simulation (continuous blue line) at the same location. The comparison is only valid before the instant 7 ps indicated by the dashed red line because, after this instant, the reflections originated at the faces of the substrate reach the antenna and cause interference in the simulation. As we explain in section 3, the substrate in the numerical model has been designed significantly smaller than the real substrate employed in the laboratory experiment, in order to reduce the computational load; as a consequence the reflections are detected earlier in the simulation than in the real experiment.

#167707 - $15.00 USD Received 1 May 2012; revised 13 Jun 2012; accepted 14 Jun 2012; published 29 Jun 2012

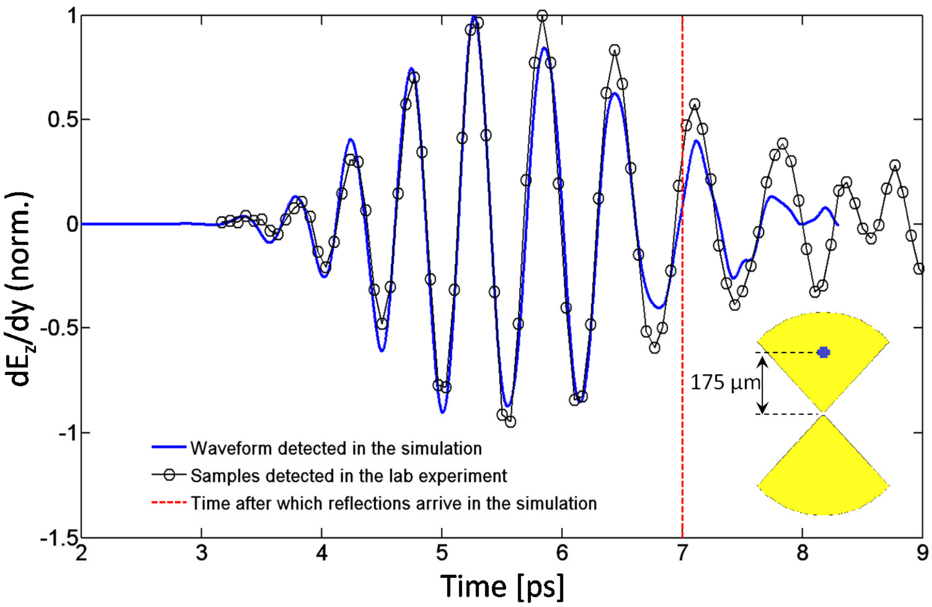

Fig. 5. Comparison between the time-domain waveform detected in the laboratory experiment (black circles) on the metal of the antenna at a distance of 175 µm from the centre of the gap and the time-domain waveform of the electric field z component spatial derivative $dE_z(t)/dy$ obtained in the simulation (continuous blue line) at the same location (shown in the inset). The comparison is only valid before the instant 7 ps, indicated by the dashed red line; after this instant the reflections from the faces of the substrate reach the antenna and cause interference in the simulation.

The mapping of the field distribution on THz antennas allows application of near-field imaging in further studies of antenna analysis and design. For instance it would be important to establish whether and how the patterns mapped with the probes can be related to intrinsic properties of the antennas. In our future work we will perform a thorough study about the invasiveness of the probe and how to extract from our measurement the information concerning the real scenario without the presence of the probe. In order to carry out a first assessment of the invasiveness of the probe on the surface plasmon wave during the considered window of time, we run a second simulation to calculate the distribution of the electric field over the antenna when the probe is not present. The z_{max} boundary condition over the antenna is therefore changed to “open (add space)”.

The comparison between the electric field z component on the antenna at the time t_1, t_2, t_3, t_4 with and without the probe is illustrated in Fig. 6. The presence of the metallic plane 3 µm over the antenna seems to support the normal component of the electric field resulting in larger values of the field, as is evident from the scale on the colour bars in Fig. 6. The difference in amplitude is though not important as long as the pattern of the electric field distribution is not affected significantly by the probe. The colours in the case without probe have been saturated to highlight the distribution pattern and allow a comparison. Apart from a border effect, that is worth further investigation, the distribution of the electric field within this early window of time has not changed significantly, with maxima and minima still present in the same locations.

#167707 - $15.00 USD Received 1 May 2012; revised 13 Jun 2012; accepted 14 Jun 2012; published 29 Jun 2012

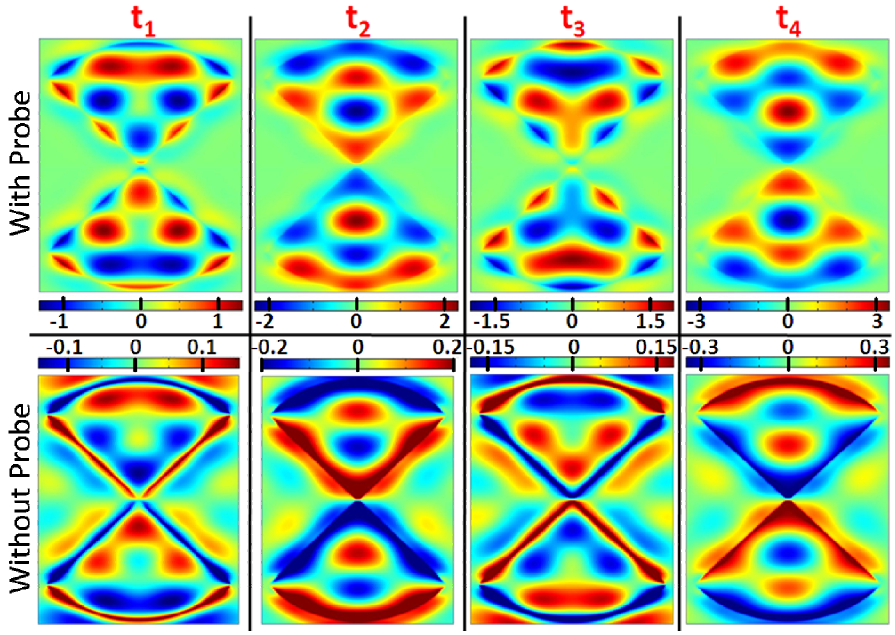

Fig. 6. Comparison between the simulated E_z component on the antenna at the times t_1, t_2, t_3, t_4 with and without the probe. The scale in the case without the probe has been saturated to highlight the distribution pattern and allow a comparison.

5. Conclusion

The response of the integrated sub-wavelength aperture probe has been modelled and measured for the case of a bow-tie THz antenna on a dielectric substrate. The simulation results provide, for the first time, conclusive demonstration that the physical quantity detected by the probe is the spatial derivative of the electric field normal component. The achieved full understanding of the near-field probe response allows now a correct interpretation of the images and the distribution of the electric field to be extracted.

A preliminary assessment of the invasiveness of the probe within the considered window of time, with respect to the field distribution, has also been carried out for the first time, by running two numerical simulations with different boundary conditions over the antenna. The "border effect" introduced by the probe does not modify significantly the field distribution on the surface of the antenna but needs additional explanation and will be further investigated. Some of the future research work will perform a thorough study about the invasiveness of the probe and try to establish whether and how the patterns mapped with the probes can be related to intrinsic properties of the antennas, which would provide, among other things, effective new tools to assist THz antenna analysis and design.

#167707 - $15.00 USD Received 1 May 2012; revised 13 Jun 2012; accepted 14 Jun 2012; published 29 Jun 2012